EDGE ARTICLE

Check for updates

"Dual lock-and-key" triggered and endoplasmic reticulum targeting nanophotosensitizers for activatable Type-I photodynamic and photothermal therapies†

Rumeng Zhan,[a] Weijie Zhou,[a] Hongyu Ma,[a] Menghui Zou,[a] Mingming Zhang, [ID] *[b] Weian Zhang [ID] *[a] and Jia Tian [ID] *[a]

Photodynamic therapy (PDT) has emerged as a critical modality in cancer treatment with the merits of non-invasiveness, spatiotemporal control, and minimal drug resistance. However, the clinical application of PDT is often hindered by inherent limitations, including side effects caused by the "always on" state of reactive oxygen species (ROS) and low ROS generation efficiency in hypoxic tumors. To overcome these limitations, we developed a tumor microenvironment (TME) "dual lock-and-key" triggered and endoplasmic reticulum (ER) targeting nanophotosensitizer for fluorescence imaging-guided activatable Type-I PDT and photothermal therapy (PTT). This "smart" nanophotosensitizer remains in an "off" state during systemic circulation, and is specifically activated only in the acidic and GSH-overexpressed TME ("on" state), where its fluorescence, ROS generation, and photothermal conversion capabilities are restored, leading to precise and enhanced phototherapies at tumor sites while minimizing side effects. Sulfur-substituted and ER-targeting hemicyanine induces a large red-shift in absorption, simultaneously generating Type-I ROS and producing a photothermal effect in the ER, thereby enhancing protein deactivation and ER stress. Comprehensive *in vitro* and *in vivo* investigations demonstrated that the TME dual triggered activatable nanophotosensitizer, upon NIR laser irradiation, effectively kills tumor cells, and significantly suppresses tumor growth through fluorescence imaging-guided Type-I PDT and PTT. This work provides a pathway for developing TME-triggered precise phototherapeutics with improved biosafety and potential for clinical translation.

Introduction

Photodynamic therapy (PDT) has emerged as a highly effective anticancer strategy, utilizing photosensitizers (PSs) to generate cytotoxic reactive oxygen species (ROS) to kill tumors upon light irradiation.[1–8] Compared to conventional treatments like surgery, chemotherapy, and radiotherapy, PDT exhibits distinct advantages including non-invasiveness, spatiotemporal control, and minimal drug resistance.[9–13] However, the "always on" state of ROS results in systematic side effects such as skin sensitization, swelling, and organ damage.[14–16] The development of activatable nanophotosensitizers provides the opportunity to significantly reduce the systematic side effects of

PDT.[17,18] These intelligent nanophotosensitizers remain in a quenched "off" state in blood circulation and healthy tissues and can only be activated upon encountering specific stimuli.[19] The specific tumor microenvironment (TME), characterized by dysregulated enzymes,[20] hypoxia,[21] redox imbalances,[22] and acidic pH,[23] plays an essential role in dynamically modulating cancer progression and influencing the outcomes of cancer treatment.[24,25] TME-triggered activatable nanophotosensitizers represent one of the most promising strategies, providing obvious advantages in boosting the therapeutic efficacy in tumor sites while minimizing side effects.[26,27] Although extensive efforts have been devoted to the construction of TME-triggered nanophotosensitizers, most of them have focused on single-pathological parameter activatable nanophotosensitizers, which are insufficient to distinguish the complex and dynamic TME, potentially resulting in nonspecific activation and even "false positive" results.[28] Thus, it is more effective and practical to develop activatable nanophotosensitizers relying on cooperative activation by multi-pathological parameters, which significantly reduces interference signals from normal tissues. However, difficulties

[a]Shanghai Key Laboratory of Functional Materials Chemistry, School of Chemistry and Molecular Engineering, East China University of Science and Technology, Shanghai 200237, China. E-mail: wazhang@ecust.edu.cn; tianjia@ecust.edu.cn
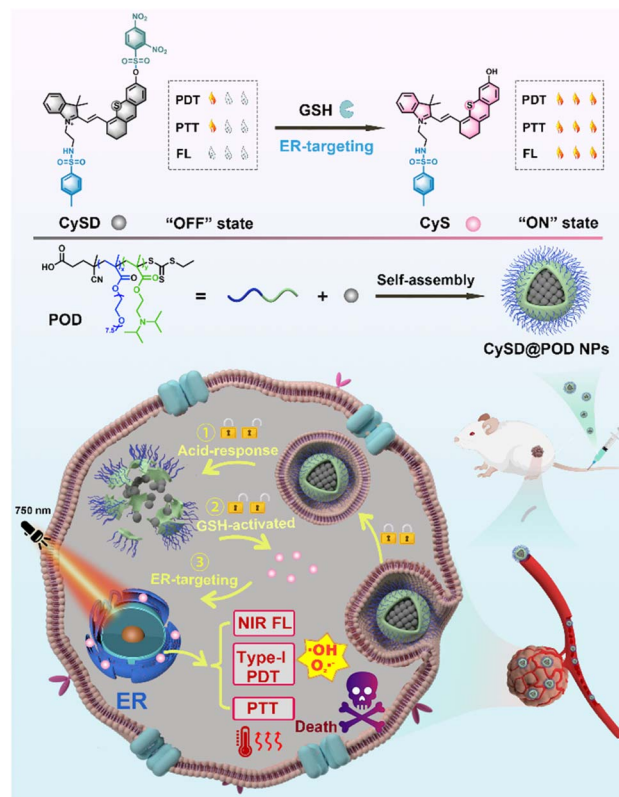
[b]Tianjin Key Laboratory of Biomedical Materials, Institute of Biomedical Engineering, Chinese Academy of Medical Sciences, Peking Union Medical College, Tianjin 300192, China. E-mail: zhangmm@bme.pumc.edu.cn

† Electronic supplementary information (ESI) available. See DOI: https://doi.org/10.1039/d5sc01987g

in molecular design and complex synthesis limit the development of nanophotosensitizers that are collectively activatable by multi-pathological-parameters.

The synthetic accessibility of hemicyanine dyes, coupled with their distinctive donor–π–acceptor (D–π–A) architecture and NIR absorption/emission characteristics, establishes an ideal foundation for developing activatable nanophotosensitizers.[29–31] A lot of hemicyanine dyes with different functions have been explored, exhibiting promising potential in tumor diagnosis and treatment.[32–34] These systems offer distinct advantages over conventional cyanine-based dyes (such as Cy7 and ICG), including reduced molecular dimensions, enhanced structural stability, and improved biocompatibility.[35] The intramolecular charge transfer (ICT) process between donor and acceptor moieties facilitates Type-I ROS generation, NIR fluorescence modulation, and versatile functionalization, enabling significant advancements in biomarker-targeted hemicyanine-based activatable nanophotosensitizers.[36–38] However, the visible light absorption of hemicyanine limits the tissue permeation of light, which significantly decreases the phototherapeutic efficacy of hemicyanine. Recent structural optimization strategies, particularly oxygen-to-sulfur substitution, have demonstrated a significant red-shift in absorption and enhanced photothermal conversion efficiency, enabling near-infrared absorption induced deeper tissue penetration, and synergistic PDT/PTT within a single molecular framework.[39,40] Thus, the construction of an activatable nanophotosensitizer based on sulfur-substituted hemicyanine with an orthogonal and pathological parameter-responsive vehicle provides a promising and versatile strategy for precise and activatable combined photodynamic and photothermal therapies (Scheme 1).

Herein, we report a "dual lock-and-key" controlled and endoplasmic reticulum (ER)-targeting nanophotosensitizer (denoted as CySD@POD) for NIR fluorescence-guided activatable phototherapies. The "smart" nanophotosensitizer consists of a pH-responsive polymeric vehicle (POD) and a sulfur-substituted hemicyanine photosensitizer (CySD) with 2,4-dinitrobenzenesulfonyl (DNBS) as a quenching unit and 4-methylbenzenesulfonamide as an ER-targeting unit. The "dual lock-and-key" controlled and ER-targeting nanophotosensitizer CySD@POD possesses the following advantages: (1) The pH and over-expressed GSH in the TME act as two independent activation keys for the dual locked nanophotosensitizer, which turn on fluorescence, as well as photodynamic and photothermal therapeutic functions, leading to precise cancer treatment and reduced side effects. (2) ER-targeting Type-I PDT of the nanophotosensitizer not only overcomes the dependence of PDT on oxygen levels, but also enhances the ER stress via ROS generated during PDT, giving rise to enhanced PDT. (3) The sulfur-substitution of hemicyanine results in a red-shift of the maximum absorption to the NIR window and strong photothermal capability, promoting tissue penetration and enhancing phototherapeutic outcomes by combined NIR Type-I PDT and PTT. The pH/GSH dual-triggered activation of fluorescence, ROS, and heat generation of CySD@POD were explored. Comprehensive in vitro and in vivo evaluations were

Scheme 1 Schematic diagram of the synthesis and therapeutic process of "dual lock-and-key" triggered and endoplasmic reticulum targeting nanophotosensitizers with pH/GSH dual-triggered activation of near infrared fluorescence, photothermal, and photodynamic properties.

performed to verify ER-specific localization, phototoxicity, and potent tumoricidal efficacy. The TME dual-activated Type-I nanophotosensitizer provides a promising pathway for precise cancer treatment.

Results and discussion

Synthesis and GSH-activated properties of CySD

The phototherapeutic agent CySD consists of three parts, incorporating hemicyanine as the fluorophore core, a 4-methylbenzenesulfonyl group for ER targeting, and DNBS as the quenching and GSH-activated moiety. The synthetic processes are provided in Scheme S1 (ESI†). CyS, which was first synthesized by the coupling of hemicyanine and ER-targeting moieties, exhibits strong NIR absorption and fluorescence. When CyS was linked with the quenching unit DNBS, the resulting CySD shows blue shifted absorption and limited fluorescence (Fig. 1A and B). The chemical structures of CySD, intermediate compounds, the oxygen-substituted hemicyanine Cy–O–OH and the sulfur-substituted hemicyanine Cy–S–OH were confirmed by detailed comprehensive characterization, including ^{1}H NMR, ^{13}C NMR, and high-resolution mass spectrometry (Scheme S2 and Fig. S1–S13†). The optical properties of Cy–O–OH and Cy–S–OH were analysed and compared. The corresponding
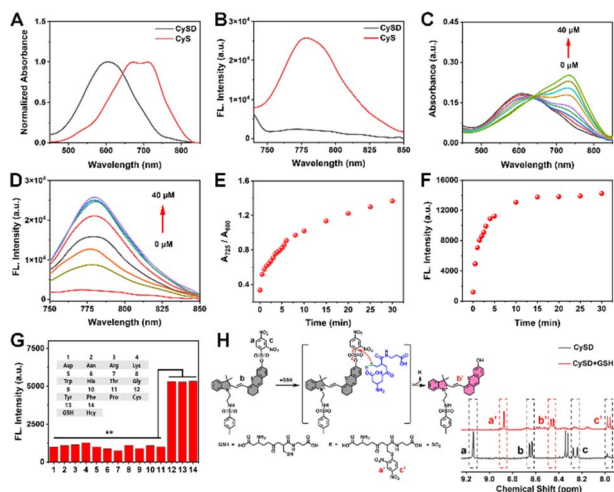
Fig. 1 (A) The normalized UV-vis absorption spectra and (B) the fluorescence spectra of CyS and CySD. (λ_{ex}: 720 nm). (C) The UV-vis absorption spectra and (D) the fluorescence spectra changes of CySD (20 µM) in response to different concentrations of GSH. (E) Variation of absorbance at 725 nm and (F) fluorescence intensity at 780 nm of CySD (20 µM) with response time to GSH (20 µM). (G) The selectivity experiments of CySD (5 µM) toward biothiols and various amino acids (100 µM). (H) ^{1}H NMR spectrum of CySD in response to GSH.

chemical structures of Cy–O–OH and Cy–S–OH are provided in Fig. S14A.† Moreover, the comparison of optical properties between Cy–S–OH and Cy–O–OH is presented in Fig. S14B–P.† It is obvious that Cy–S–OH possesses red-shifted absorption and fluorescence wavelengths, and greater ROS generation capability than Cy–O–OH. Moreover, density functional theory (DFT) was used to study the optical behavior of Cy–S–OH. It was revealed that the sulfur-substituted hemicyanine exhibits a lower HOMO–LUMO energy gap and a lower singlet–triplet energy gap than its oxygen-substituted counterpart (Fig. S15†), indicating a higher ISC rate and better ROS generation in PDT compared to Cy–O–OH. The results were consistent with previous publications,[40–42] in which Cy–S–OH exhibited a lower fluorescence quantum yield, and higher singlet oxygen quantum yield and photothermal conversion efficiency than Cy–O–OH.

GSH, a key intracellular reducing agent, is significantly overexpressed in the TME, with concentrations often exceeding 4 times than those in normal cells.[43,44] The GSH-activated behavior of CySD was evaluated. A concentration-dependent conversion from CySD to CyS was observed from UV-vis absorption spectra, where the absorbance at 600 nm decreased while the absorbance at 725 nm increased progressively with GSH concentration (Fig. 1C and S16†). Corresponding fluorescence spectra demonstrated a gradual enhancement in emission intensity of CySD with increasing GSH levels, confirming the sensitive activation of CySD and its potential as a TME-activated PS (Fig. 1D and S17†). Meanwhile, CySD presents a rapid temporal response to GSH, confirmed by the rapidly increased absorption at 725 nm and fluorescence emission at 780 nm, reaching saturation within 30 minutes, suggesting that CySD can be efficiently activated by GSH (Fig. 1E, F, S18 and S19†). Selectivity studies showed that GSH and

similar thiols such as cysteine (Cys) and homocysteine (Hcy) induced increased fluorescence (Fig. 1G). In contrast, other amino acids, such as Asp, Asn, and Arg, failed to induce fluorescence activation. Given the elevated levels of biothiols, particularly GSH, in tumor cells, these results suggest significantly higher selectivity of CySD in cancer cells than normal cells. The reaction mechanism between CySD and GSH was further elucidated from the ^{1}H NMR spectrum (Fig. 1H). Upon GSH addition, CySD undergoes nucleophilic substitution with the sulfhydryl group, leading to the release of the DNBS moiety. This is evidenced by significant upfield shifts in the proton signals of CySD and DNBS. The strong electron-withdrawing group DNBS initially inhibits the ICT process of CySD. Upon DNBS cleavage, the charge transfer within the fluorophore molecule is restored, resulting in fluorescence recovery. This mechanism underscores the design rationale for the activatable behavior of CySD in the TME.

The photodynamic and photothermal properties of CySD could be effectively triggered by GSH nucleophilic substitution and subsequent DNBS cleavage. There are generally two types of PDT: Type-I PDT produces hydroxyl radicals or superoxide anion radicals through electron transfer or hydrogen abstraction-based photoreactions once the photosensitizer absorbs photons, and Type-II PDT generates singlet oxygen *via* an energy transfer mechanism. Thus, Type-I PDT is less dependent on the availability of O_2, which is promising in hypoxic tumor treatment.[45] 3,3′,5,5′-Tetramethylbenzidine (TMB) and dihydroethidium (DHE) were used as specific probes to detect the generated ·OH and $O_2^{-\bullet}$, respectively.[46] Upon GSH addition, the absorbance at 650 nm for TMB solution containing CySD under 750 nm light irradiation increased 11-fold, demonstrating substantial ·OH production by the GSH-activated Type I photodynamic reaction of CySD under laser irradiation (Fig. 2A and S20†). Similarly, the fluorescence of DHE significantly enhanced in the presence of GSH, confirming robust $O_2^{-\bullet}$ generation by GSH-activated photodynamic properties of CySD (Fig. 2B and S21†).
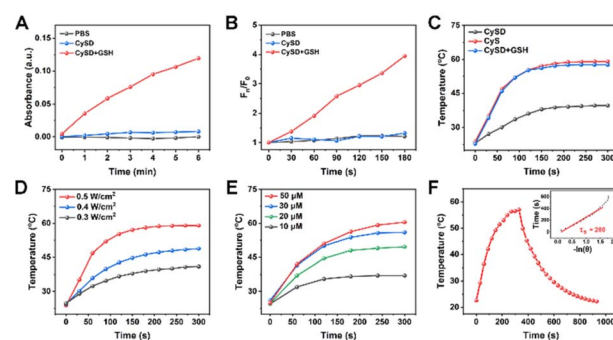

Fig. 2 (A) Absorbance variation of TMB at 650 nm with PBS, CySD and CySD + GSH under light irradiation at predetermined time points. (B) Fluorescence intensity changes of DHE at 610 nm with PBS, CySD and CySD + GSH under light irradiation at predetermined time points. Laser: 750 nm, 0.1 W cm^{-2}. (C) Photothermal heating curves of PBS, CySD and CySD + GSH under light irradiation. Photothermal heating curves of CySD + GSH (D) at different laser powers and (E) concentrations. (F) The heating and cooling curves of CySD + GSH. Laser: 750 nm, 0.5 W cm^{-2}.

The photothermal properties of CySD were evaluated before and after GSH activation. The photothermal performance of CySD was markedly reduced because of the introduction of DNBS, with the solution temperature increasing by only 16 °C (from 23 to 39 °C) under light irradiation. In contrast, GSH-activated CySD solution exhibited a dramatic temperature rise of 34 °C (from 23 to 57 °C), achieving photothermal performance comparable to that of CyS (Fig. 2C). Further characterization revealed that the GSH-triggered photothermal performance of CySD was concentration- and laser power-dependent, with the GSH-activated system demonstrating a calculated photothermal conversion efficiency of 37.7% (Fig. 2D–F). Moreover, the photostability of CySD in GSH solution was assessed through a heating–cooling process. After three heating–cooling circles, the increased temperature still remained above 50 °C (Fig. S22†), indicating the good photostability of CySD in a GSH-rich environment. These results collectively demonstrate that CySD functions as a GSH-triggered phototherapeutic agent with both Type I photodynamic and photothermal capabilities, making it a promising candidate for precise cancer therapy in the GSH-overexpressed TME.

Preparation and acid-responsive properties of CySD@POD

Although CySD exhibits excellent GSH-activated photodynamic and photothermal properties, its clinical application is hindered by its poor tumor targeting, low aqueous solubility, and short circulation time. To address these challenges, an acid-responsive amphiphilic block copolymer, POD, was prepared *via* RAFT polymerization and utilized as a TME-responsive vehicle. The synthesis and characterization of POD are presented in Scheme S3 and Fig. S23 and S24†, respectively. Subsequently CySD@POD nanoparticles were obtained through nanoprecipitation of CySD and POD. The resulting nanoparticles feature a core–shell structure, with hydrophilic POEGMA chains forming the outer shell and hydrophobic DPA blocks encapsulating CySD in the core. Under acidic conditions (pH < 7), the protonation of tertiary amine groups in POD triggers a hydrophilic transition, leading to nanoparticle dissociation (Fig. 3A). UV-vis absorption spectra of CySD@POD exhibited the characteristic absorption peak of CySD at 600 nm, indicating the successful loading of CySD (Fig. 3B). Dynamic light scattering (DLS) analysis revealed a hydrodynamic diameter of 150 nm, while the transmission electron microscopy (TEM) image demonstrated a uniform spherical morphology (Fig. 3C). Stability studies in PBS (pH = 7.4) showed no significant changes in hydrodynamic diameter or polydispersity index (PDI) over one week, confirming excellent colloidal stability (Fig. S25†).

The pH-triggered dissociation behavior of CySD@POD nanoparticles was investigated. The DLS curve of CySD@POD nanoparticles at pH 5.5 showed a bigger hydrodynamic size and a bimodal size distribution; the TEM image also revealed an irregular morphology (Fig. 3D). The standard curve of CySD was established based on the absorbance at 600 nm (Fig. S26†). The
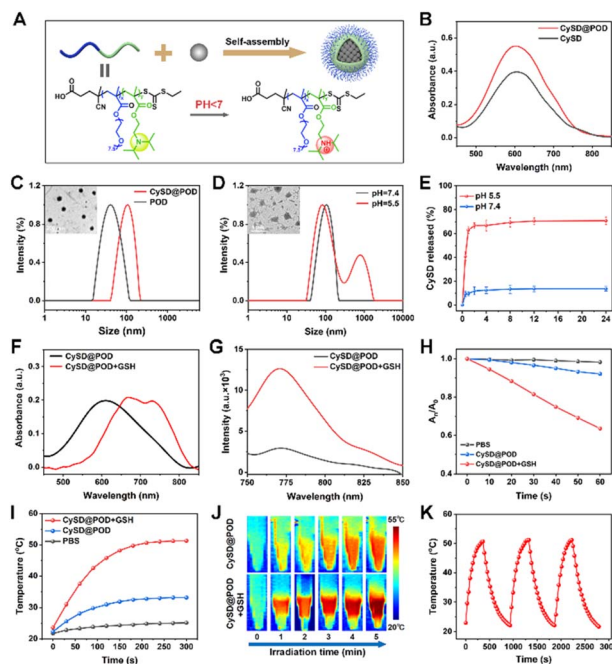

Fig. 3 (A) Schematic illustration of the pH–responsive release of CySD@POD assemblies. (B) UV-vis absorption curves of CySD and CySD@POD. Hydrodynamic size distributions and the inset shows the TEM image of CySD@POD in PBS solution at (C) pH = 7.4 and (D) pH = 5.5. (E) CySD release profiles of CySD@POD at different pH values. (F) UV-vis absorption spectra and (G) fluorescence spectra of CySD@POD before and after response to GSH. (H) Absorbance variation of DPBF at 425 nm with PBS, CySD@POD and CySD@POD + GSH under light irradiation at predetermined time points. Laser: 750 nm, 0.1 W cm^{-2}. (I) Photothermal heating curves of PBS, CySD@POD and CySD@POD + GSH in PBS. (J) Photothermal images of CySD@POD before and after response to GSH under light irradiation. (K) Three cycles of heating–cooling processes of CySD@POD + GSH. Laser: 750 nm, 0.5 W cm^{-2}.

loading efficiency of CySD in CySD@POD was calculated to be *ca.*71% (Fig. 3E). Furthermore, the absorption of CySD@POD decreased with prolonged acid exposure time, potentially due to the precipitation of released CySD in PBS (Fig. S27†). These results collectively demonstrate the acid-triggered disassembly of CySD@POD nanoparticles, highlighting their potential for acidic TME-triggered drug delivery.

pH and GSH dual-triggered activation of photodynamic and photothermal properties of CySD@POD

The pH and GSH dual-triggered activation of the optical properties of CySD@POD nanoparticles was subsequently investigated. As anticipated, the maximum absorption peak of CySD@POD solution exhibited a characteristic red shift from 600 nm to 725 nm following exposure to both weak acidity and GSH (Fig. 3F). Concurrently, the dual pH/GSH activation induced a remarkable 5-fold increase in fluorescence intensity, transitioning from a nearly non-fluorescent state to strong emission (Fig. 3G). The fluorescence quantum yields (QYs) of CyS, CySD, and CySD@POD were determined to be 0.11%, 0.005%, and 0.004%, respectively. These results validate that

the double locked CySD@POD nanoparticles need both weak acidity and GSH as two keys for the activation of optical properties, highlighting their potential for safe and precise cancer treatment in the specific acidic and GSH-overexpressed TME.

1,3-Diphenylisobenzofuran (DPBF) was employed as a ROS detection probe.[47] The absorbance of DPBF at 425 nm decreased more rapidly in the presence of pH/GSH dual-activated CySD@POD, demonstrating enhanced ROS production capacity upon activation (Fig. 3H and S28†). Photothermal performance evaluation revealed a substantial temperature increase of 25.5 °C for pH/GSH-activated CySD@POD, compared to only 10.8 °C for CySD@POD alone (Fig. 3I). These findings were corroborated by infrared thermal imaging, which visually demonstrated the enhanced photothermal effect of pH/GSH-activated CySD@POD under laser irradiation (Fig. 3J and S29†). In addition, no decrease in the maximum temperature of the mixed solution of CySD@POD nanoparticles and GSH was observed after three heating–cooling cycles (Fig. 3K), indicating the excellent photostability of CySD@POD nanoparticles even at high GSH levels. The combined Type-I PDT and PTT of activated CySD@POD can exhibit outstanding tumor killing effects, since ROS produced in PDT could deactivate the heat shock proteins (HSP) generated during PTT, and the heating and Type I PDT reactions overcome the oxygen-dependence of traditional PDT.[48,49] The observed "off–on" fluorescence transition, coupled with pH/GSH-activated photodynamic and photothermal capabilities, positions CySD@POD as a promising theranostic platform for imaging-guided phototherapies.

ER localization and ROS production of CySD@POD *in vitro*

Building on the demonstrated pH and GSH dual-triggered activation properties of CySD@POD, *in vitro* studies was next investigated. Cellular uptake of CySD@POD was evaluated by confocal laser scanning microscopy (CLSM) to compare internalization between tumor cells (B16-F10 mouse melanoma) and normal cells (L929 mouse fibroblasts). As shown in Fig. 4A, B16-F10 cells demonstrated time-dependent fluorescence enhancement, while L929 cells exhibited negligible red fluorescence after 12 h of incubation, confirming enhanced tumor cellular uptake and TME-triggered activation of CySD@POD (Fig. S30†). The ER-targeting capability of CySD@POD, mediated thourgh 4-toluenesulfonyl group interactions with sulfonylurea receptors on the ER membrane, was confirmed *via* colocalization with ER Tracker Green (a commercially available ER-specific fluorescent probe). CLSM imaging of B16-F10 cells incubated with CySD@POD for 24 h revealed strong colocalization (Pearson's coefficient = 0.96) between the green ER marker and red CySD@POD fluorescence (Fig. 4B and S31†). The fluorescence intensity profile further confirmed precise ER localization, with overlapping red and green fluorescence patterns (Fig. 4C).[50] This targeted delivery is particularly significant given the critical role of the ER in maintaining cellular homeostasis and cell death.

Intracellular ROS generation was evaluated using 2′,7′-dichlorodihydrofluorescein diacetate (DCFH-DA) as a fluorescent probe in B16-F10 tumor cells.[51] Bright green fluorescence
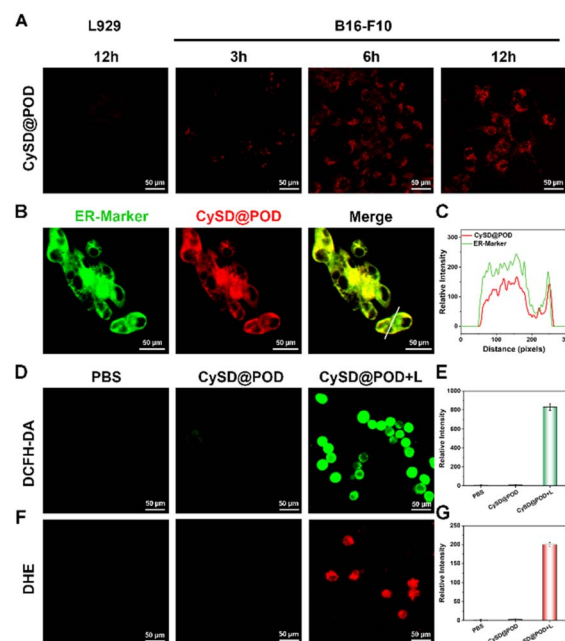

Fig. 4 (A) Confocal fluorescence images of CySD@POD incubation in L929 and B16-F10 cells at different time points. (B) Confocal fluorescence images of B16-F10 cells co-stained with CySD@POD (5 μM, λ_{ex} = 561 nm and λ_{em} = 600 ± 26 nm) and commercial dyes ER Tracker Green (0.5 μM, λ_{ex} = 488 nm and λ_{em} = 525 ± 25 nm). (C) Linear analysis of selected regions in confocal fluorescence images. (D) Detection of intracellular ROS in B16-F10 cells using DCFH-DA (λ_{ex} = 488 nm and λ_{em} = 525 ± 25 nm). (E) Quantification of green fluorescence intensity from DCFH-DA stained fluorescence images. (F) Detection of intracellular O_2^- in B16-F10 cells using DHE (λ_{ex} = 561 nm and λ_{em} = 750 ± 50 nm). (G) Quantification of red fluorescence intensity from DHE stained fluorescence images. Scale bar: 50 μm. Laser: 750 nm, 0.1 W cm^{-2}, 5 min.

in the CySD@POD + L group contrasted sharply with the control groups, demonstrating efficient ROS production by activated CySD@POD in tumor cells (Fig. 4D and E). Furthermore, intracellular O_2^-· generation was evaluated using DHE as the probe. Upon light irradiation, bright red fluorescence was observed in the cells treated with CySD@POD nanoparticles (Fig. 4F), and comparison of relative fluorescence intensity illustrated that CySD@POD possessed excellent Type-I photodynamic activity in tumor cells upon light irradiation (Fig. 4G). The accumulation of excessive ROS within the ER induces ER stress, which at severe levels triggers apoptotic pathways; thus the dual-locked TME-triggered phototherapeutic system CySD@POD provides a mechanism for specific tumor cell destruction while minimizing off-target effects.

In vitro cytotoxicity of CySD@POD

Encouraged by the excellent intracellular ROS generation capability and ER localization of CySD@POD, the *in vitro* cytotoxicity of CySD@POD was evaluated using 3-(4,5-dimethylthiazol-2-yl)-2,5-diphenyltetrazolium bromide (MTT) assay.[52] As shown in Fig. 5A, CySD@POD demonstrated excellent cytocompatibility with normal cells (L929), maintaining over 82% cell viability across the tested concentration range. In contrast, CySD@POD

exhibited concentration-dependent phototoxicity under 750 nm light irradiation against tumor cells (B16-F10), with cell viability decreasing to 30% at 10 μM (Fig. 5B). The enhanced cytotoxicity under NIR light irradiation can be attributed to the acidic and elevated GSH levels in the TME, which act as the "dual lock-and-key", triggering the activation of CySD@POD, and leading to cellular photodamage. In addition, it has been reported that the combination of ER targeting and high levels of ROS in PDT could induce serious oxidative damage to the ER of tumor cells, leading to ER stress, cell apoptosis and pyroptosis.[53–55] Thus, the control sample, CySH@POD nanoparticles, was prepared through the co-assembly of sulfur-substituted hemicyanine Cy–S–OH and POD, possessing no endoplasmic reticulum targeting ability. And the cytotoxicity of CySH@POD and CySD@POD nanoparticles against B16-F10 tumor cells were evaluated under identical conditions. Compared with cells treated with the ER-targeting CySD@POD nanoparticles, those treated with CySH@POD exhibited significantly higher cell viability upon light irradiation, indicating that the incorporation of endoplasmic reticulum-targeting functionality significantly enhances the tumor cell-killing efficacy of the nanophotosensitizer. Notably, CySD@POD nanoparticles exhibited outstanding tumor cell-killing capability even under hypoxic conditions, owing to the combined benefits of ER targeting, activated Type-I photodynamic and photothermal effects (Fig. 5C).

To visualize the therapeutic effects, live–dead cell staining was performed using calcein AM (green channel, staining live cells) and propidium iodide (PI, red channel, staining dead cells). CLSM images revealed that B16-F10 cells treated with CySD@POD in the dark exhibited predominantly green
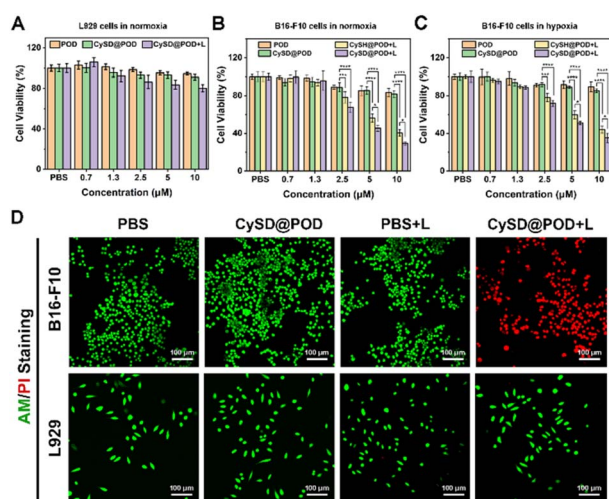

Fig. 5 (A) The cell viability of POD, CySD@POD, and CySD@POD + L in L929 cells under normoxic conditions. (B) The cell viability of POD, CySD@POD, CySH@POD + L, and CySD@POD + L in B16-F10 cells under normoxic conditions. (C) The cell viability of POD, CySD@POD, CySH@POD + L, and CySD@POD + L in B16-F10 cells under hypoxic conditions. (D) Calcein AM (green) and PI (red) co-staining fluorescence imaging of B16-F10 and L929 cells after different treatments. Scale bar: 100 μm. Laser: 750 nm, 0.5 W cm^{-2}, 5 min. *$p < 0.05$, ***$p < 0.001$, and ****$p < 0.0001$.

fluorescence, confirming the minimal cytotoxicity of CySD@POD without light irradiation (Fig. 5D). The PBS + L group serving as the control confirmed the safety of the irradiation parameters. Under 750 nm light irradiation, B16-F10 cells treated with CySD@POD showed intense red fluorescence, indicating widespread cell death, while L929 cells remained viable under the same conditions. These results demonstrate the exceptional phototherapeutic selectivity of CySD@POD, with strong tumor-killing efficiency under NIR irradiation and minimal off-target effects, highlighting its potential for activatable and precise cancer phototherapies.

In vivo phototherapy evaluation

The in vivo therapeutic efficacy of CySD@POD was evaluated. A xenograft tumor model was established by subcutaneously injecting B16-F10 cells into BALB/c mice. The mice were randomly divided into four treatment groups: (1) PBS injection alone (PBS), (2) PBS injection with laser irradiation (PBS + L), (3) CySD@POD injection alone (CySD@POD), and (4) CySD@POD injection with laser irradiation (CySD@POD + L). The treatment processes and timeline are illustrated in Fig. 6A. The biodistribution and tumor accumulation of CySD@POD were preferentially assessed and monitored using an in vivo imaging system. As shown in Fig. 6B, fluorescence at the tumor site increased progressively over time, indicating that CySD@POD nanoparticles effectively accumulated at the tumor site via the EPR effect, disassembled and released the phototherapeutic agent CyS. The fluorescence intensity profiles of CySD@POD in the tumor sites at different time points were plotted, as shown in Fig. S32.† The maximum fluorescence intensity was observed at 24 h post-injection, establishing this time point as the optimal window for laser irradiation.

To further quantify the biodistribution, tumors and major organs were harvested 24 h post-injection of CySD@POD and and subjected to ex vivo fluorescence imaging (Fig. S33†). The tumor exhibited the highest fluorescence intensity, followed by the liver and spleen, confirming efficient tumor accumulation and subsequent clearance through hepatic and splenic pathways. These results underscore the tumor-specific accumulation and favorable pharmacokinetics of CySD@POD, supporting its potential for precise phototherapies with enhanced biosafety.

The therapeutic efficacy of CySD@POD was evaluated by monitoring tumor volumes over a 14-day treatment period. As shown in Fig. 6C, rapid tumor growth was observed in the PBS, PBS + L, and CySD@POD groups, with tumor volumes increasing 5-fold approximately by day 14, confirming that neither laser irradiation alone nor CySD@POD without light irradiation could inhibit tumor progression. In contrast, the CySD@POD + L group exhibited significant tumor suppression under laser irradiation, demonstrating the outstanding phototherapeutic efficacy of CySD@POD with both TME-activation and light irradiation. On day 14, tumors were excised and weighed, with the CySD@POD + L group showing the smallest tumor mass, further validating its potent antitumor effects (Fig. 6D). Notably, no significant body weight loss was observed
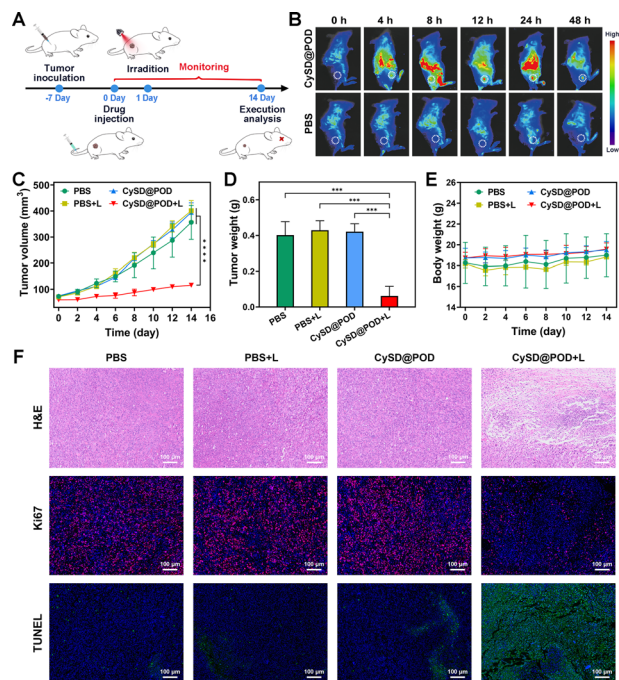
Fig. 6 (A) Schematic diagram showing the process of *in vivo* tumor studies in mice. (B) *In vivo* fluorescence imaging of mice after subcutaneous injection with CySD@POD. (C) The relative tumor volume in four groups including PBS, PBS + L, CySD@POD, and CySD@POD + L. Error bars, mean ± SD ($n = 3$). (D) Average weight of tumor at day 14 after treatment. (E) Body weight changes of mice in different treatment groups. Error bars, mean ± SD ($n = 3$). (F) H&E, Ki67 and TUNEL staining of tumor tissues collected from mice in different groups after treatment. Scale bar: 100 μm. Laser: 750 nm, 0.5 W cm^{-2}, 5 min. ***$p < 0.001$, and ****$p < 0.0001$.

across all treatment groups, underscoring the excellent biosafety profile of CySD@POD (Fig. 6E).

Histopathological analysis of tumor tissues provided additional support for assessing the therapeutic efficacy of CySD@POD. Hematoxylin and eosin (H&E) staining revealed extensive tumor cell destruction in the CySD@POD + L group compared to the control groups (Fig. 6F). Immunohistochemical staining for Ki67 (a proliferation marker) and TUNEL (an apoptosis indicator) confirmed that CySD@POD-mediated phototherapy significantly suppressed tumor cell proliferation while promoting apoptosis.

In addition, the *in vivo* metabolism of the nanophotosensitizer was assessed. Considering there's no GSH overexpression in blood and major organs, CyS@POD nanoparticles (6.0 mg kg^{-1}) were used for tail veil injection and analysis instead of CySD@POD nanoparticles.

The fluorescence changes of CyS@POD in blood over time after tail veil injection were plotted, as shown in Fig. S34.† The results revealed that the drug concentration reached the maximum after 1 h of administration in mice. With the passage of time, the blood concentration gradually decreased and the drug was completely eliminated after 24 h of administration, indicating that CyS@POD can be stably metabolized in the blood. In addition, the fluorescence of CyS@POD was mainly distributed in the liver, and decreased substantially in main

organs after 48 h (Fig. S35†), demonstrating that the nanophotosensitizer was efficiently metabolized through the organs with low long-term toxicity. To further assess systemic safety, H&E staining of major organs (heart, lungs, spleen, kidneys, and liver) was performed, showing no evidence of significant tissue damage or pathological abnormalities in any treatment group (Fig. S36†). These findings collectively demonstrate that the combined PDT and PTT effects of CySD@POD in the TME integrate exceptional biocompatibility with potent tumor-killing capabilities, highlighting its strong potential for clinical application in cancer treatment.

Conclusions

In summary, a TME "dual-lock and key" triggered nanophotosensitizer, CySD@POD, was developed for activatable combined photodynamic and photothermal therapies. Upon exposure to acidic GSH solution, the fluorescence, ROS generation, and photothermal capabilities of CySD@POD were simultaneously activated, as confirmed by strong NIR fluorescence, enhanced ·OH and O_2^-· generation, and high photothermal conversion efficiency. CySD@POD exhibited effective ER-targeting with ER colocalization with the commercial ER Tracker Green reaching as high as 96%. *In vitro* studies revealed that CySD@POD nanoparticles exhibit high phototoxicity to tumor cells, with almost negligible toxicity to normal cells. Additionally, *in vivo* studies demonstrated that CySD@POD nanoparticles could accumulate at tumor sites and, upon activation by the weakly acidic and GSH-overexpressed TME, induce enhanced photodynamic and photothermal effects, thereby inhibiting tumor growth. It presents a promising approach for the development of activatable multifunctional phototherapeutic platforms.

Data availability

The data supporting this article have been included as part of the ESI.†

Author contributions

R. Z., W. Z. and J. T. conceived and designed the study. R. Z. and W. Z. performed the synthesis of the materials. R. Z., W. Z. and H. M. performed the spectral experiments and analysis. R. Z. and M. Z. performed the TEM experiments, cell culture and animal studies. R. Z., M. Z. and J. T. wrote the manuscript with contributions from all authors. J. T. and W. Z. supervised the whole project.

Conflicts of interest

There are no conflicts to declare.

Acknowledgements

animal experimental procedures were carried out in accordance with Chinese legislation regarding the Use and Care of Research Animals, and institutional guidelines for the care and use of laboratory animals established by the East China University of Science and Technology Animal Studies Committee.

Notes and references

1 J. Xie, Y. Wang, W. Choi, P. Jangili, Y. Ge, Y. Xu, J. Kang, L. Liu, B. Zhang, Z. Xie, J. He, N. Xie, G. Nie, H. Zhang and J. S. Kim, *Chem. Soc. Rev.*, 2021, **50**, 9152–9201.

2 M. Kolarikova, B. Hosikova, H. Dilenko, K. Barton-Tomankova, L. Valkova, R. Bajgar, L. Malina and H. Kolarova, *Med. Res. Rev.*, 2023, **43**, 717–774.

3 B. M. Vickerman, E. M. Zywot, T. K. Tarrant and D. S. Lawrence, *Nat. Rev. Chem.*, 2021, **5**, 816–834.

4 T. C. Pham, V.-N. Nguyen, Y. Choi, S. Lee and J. Yoon, *Chem. Rev.*, 2021, **121**, 13454–13619.

5 K.-X. Teng, L.-Y. Niu and Q.-Z. Yang, *J. Am. Chem. Soc.*, 2023, **145**, 4081–4087.

6 J. Tian, B. Li, F. Zhang, Z. Yao, W. Song, Y. Tang, Y. Ping and B. Liu, *Angew. Chem., Int. Ed.*, 2023, **62**, e202307288.

7 Z. Fan, K. Teng, Y. Xu, L. Niu and Q. Yang, *Angew. Chem., Int. Ed.*, 2025, **64**, e202413595.

8 K.-X. Teng, L.-Y. Niu and Q.-Z. Yang, *Chem. Sci.*, 2022, **13**, 5951–5956.

9 X. Li, J. F. Lovell, J. Yoon and X. Chen, *Nat. Rev. Clin. Oncol.*, 2020, **17**, 657–674.

10 W. Chen, Z. Wang, G. Hong, J. Du, F. Song and X. Peng, *Chem. Sci.*, 2024, **15**, 10945–10953.

11 C. Xu, J. Dong, X. Shi, J. Rui, M. Chen, W. Lu, A. Zhang, S. Wang, Z. Teng and X. Ye, *Acta Biomater.*, 2025, **193**, 531–544.

12 H. Wang, T. Qin, W. Wang, X. Zhou, F. Lin, G. Liang, Z. Yang, Z. Chi and B. Z. Tang, *Adv. Sci.*, 2023, **10**, 2301902.

13 R. Jin, J. Xie, X. Yang, Y. Tian, P. Yuan, Y. Bai, S. Liu, B. Cai and X. Chen, *Biomater. Sci.*, 2020, **8**, 1865–1874.

14 C. Li, L. Tu, J. Yang, C. Liu, Y. Xu, J. Li, W. Tuo, B. Olenyuk, Y. Sun, P. J. Stang and Y. Sun, *Chem. Sci.*, 2023, **14**, 2901–2909.

15 S. K. Singh and R. Singh, *Nat. Rev. Cancer*, 2022, **22**, 258.

16 N. Kwon, H. Weng, M. A. Rajora and G. Zheng, *Angew. Chem., Int. Ed.*, 2025, **64**, e202423348.

17 Q. Jiao, Y. Zheng, Q. Xie, X. Luo, S. Zhou, S. Pei, T. Zhang, X. Wu, K. Xu and W. Zhong, *Small*, 2024, **20**, 2309054.

18 H. Xu, M. Yang, Y. Du, T. Gao, Y. Liu, L. Xiong and N. Peng, *New J. Chem.*, 2022, **46**, 21235–21244.

19 C. Du, C. Wang, S.-H. Jiang, X. Zheng, Z. Li, Y. Yao, Y. Ding, T. Chen and H. Yi, *Biomater. Sci.*, 2023, **11**, 5674–5679.

20 L. Wang, T. Sun, T. Zhen, W. Li, H. Yang, S. Wang, F. Feng, Y. Chen and H. Sun, *J. Med. Chem.*, 2024, **67**, 6793–6809.

21 Y. Chen, H. Wang, X. Xu, H. Xu, B. Xiao, P. Yuan, S. Shao, W. Sun, Z. Zhou, Y. Shen and J. Tang, *Biomater. Sci.*, 2025, **13**, 1261–1271.

22 F. Zheng, D. Fan, H. Yao, J. Ding, S. Huang, Y. Fang, J. Dong, F. Chen and W. Zeng, *ACS Mater. Lett.*, 2024, **6**, 4673–4681.

23 C. Wang, Y. Tang, C. Li, W. Wu and X. Jiang, *Biomater. Sci.*, 2025, **13**, 617–626.

24 J. Wan, X. Zhang, D. Tang, T. Liu and H. Xiao, *Adv. Mater.*, 2023, **35**, 2209799.

25 S. Zeng, Z. Guo, Y. Hao, Y. S. Kafuti, Z. Yang, Q. Yao, J. Wang, X. Peng and H. Li, *Coord. Chem. Rev.*, 2024, **509**, 215786.

26 B. Niu, K. Liao, Y. Zhou, T. Wen, G. Quan, X. Pan and C. Wu, *Biomaterials*, 2021, **277**, 121110.

27 Z. Li, Z. Zhou, Y. Wang, J. Wang, L. Zhou, H.-B. Cheng and J. Yoon, *Coord. Chem. Rev.*, 2023, **493**, 215324.

28 S. Zhang, H. Chen, L. Wang, X. Qin, B. Jiang, S. Ji, X. Shen and H. Liang, *Angew. Chem., Int. Ed.*, 2022, **61**, e202107076.

29 B. Zhang, J. Lu, X. Lin, J. Wang, Q. Li, T. Jin, Q. Shi, Y. Lu, J. Zhang, J. Deng, Y. Zhang, Y. Guo, J. Gao, H. Chen, Y. Yan, J. Wu, J. Gao, J. Che, X. Dong, Z. Gu and N. Lin, *Adv. Mater.*, 2024, 2405275.

30 J. Weng, Z. Huang, Y. Liu, X. Wen, Y. Miao, J.-J. Xu and D. Ye, *J. Am. Chem. Soc.*, 2024, **146**, 13163–13175.

31 Y. Zhang, M. Zhao, J. Miao, W. Gu, J. Zhu, B. Cheng, Q. Li and Q. Miao, *ACS Mater. Lett.*, 2023, **5**, 3058–3067.

32 Z. Zeng, S. S. Liew, X. Wei and K. Pu, *Angew. Chem., Int. Ed.*, 2021, **60**, 26454–26475.

33 H. Li, H. Kim, F. Xu, J. Han, Q. Yao, J. Wang, K. Pu, X. Peng and J. Yoon, *Chem. Soc. Rev.*, 2022, **51**, 1795–1835.

34 S. Muhammad, H. Ahmad, Y. Yan, X. Chen, S. Muhammad, M. C. Maridevaru, S. Roy, Z. Wang, Y. Zhang and B. Guo, *Coord. Chem. Rev.*, 2025, **534**, 216602.

35 P. Cheng and K. Pu, *Nat. Rev. Mater.*, 2021, **6**, 1095–1113.

36 M. Zhao, Y. Zhang, J. Miao, H. Zhou, Y. Jiang, Y. Zhang, M. Miao, W. Chen, W. Xing, Q. Li and Q. Miao, *Adv. Mater.*, 2024, **36**, 2305243.

37 X. Ren, M. Tao, X. Liu, L. Zhang, M. Li and Z. Hai, *Biosens. Bioelectron.*, 2023, **219**, 114812.

38 Y. Shen, W. Li, Z. Zhou, J. Xu, Y. Li, H. Li, X. Zheng, S. Liu, X. Zhang and L. Yuan, *Angew. Chem., Int. Ed.*, 2024, **63**, e202406332.

39 Z. Cheng, S. Benson, L. Mendive-Tapia, E. Nestoros, C. Lochenie, D. Seah, K. Y. Chang, Y. Feng and M. Vendrell, *Angew. Chem., Int. Ed.*, 2024, **63**, e202404587.

40 S. Yao, Y. Chen, W. Ding, F. Xu, Z. Liu, Y. Li, Y. Wu, S. Li, W. He and Z. Guo, *Chem. Sci.*, 2023, **14**, 1234–1243.

41 M. Santra, M. Owens, G. Birch and M. Bradley, *ACS Appl. Bio Mater.*, 2021, **4**, 8503–8508.

42 X. Xia, R. Wang, Y. Hu, Q. Yao, S. Long, W. Sun, J. Fan and X. Peng, *Sci. China Chem.*, 2022, **65**, 821–828.

43 Z. Fu, D. Zhou, Z. Liu and D. Ni, *Coord. Chem. Rev.*, 2025, **533**, 216554.

44 R. Wang, M. Qiu, L. Zhang, M. Sui, L. Xiao, Q. Yu, C. Ye, S. Chen and X. Zhou, *Adv. Mater.*, 2023, **35**, 2306748.

45 M. Li, Y. Xu, X. Peng and J. S. Kim, *Acc. Chem. Res.*, 2022, **55**, 3253–3264.

46 C. Deng, M. Zheng, S. Han, Y. Wang, J. Xin, O. Aras, L. Cheng and F. An, *Adv. Funct. Mater.*, 2023, **33**, 2300348.

47 J. Zheng, W. Meng, Z. Cui, J. Tian and W. Zhang, *Biomaterials*, 2024, **311**, 122660.

48 S. Park, J.-A. Park, H. Yoo, H.-B. Park and Y. Lee, *Redox Biol.*, 2017, **13**, 470–476.

49 X. Niu, Y. Zhu, C. Ding, J. Ma, P. Wei, Y. Lin, W. Fang, Q. He, C. Li, J. Cheng, J. Zou, L. Lin, X. Chen and D. Kang, *Adv. Funct. Mater.*, 2023, **33**, 2306778.

50 H. Yao, X. Gong, M. Geng, S. Duan, P. Qiao, F. Sun, Z. Zhu and B. Du, *Biomater. Sci.*, 2022, **10**, 4008–4022.

51 X. Hu, Z. Fang, F. Sun, C. Zhu, M. Jia, X. Miao, L. Huang, W. Hu, Q. Fan, Z. Yang and W. Huang, *Angew. Chem., Int. Ed.*, 2024, **63**, e202401036.

52 N. Liu, Q. Lin, Z. Huang, C. Liu, J. Qin, Y. Yu, W. Chen, J. Zhang, M. Jiang, X. Gao, S. Huo and X. Zhu, *ACS Nano*, 2024, **18**, 7945–7958.

53 L. Zhou, F. Wei, J. Xiang, H. Li, C. Li, P. Zhang, C. Liu, P. Gong, L. Cai and K. M. C. Wong, *Chem. Sci.*, 2020, **11**, 12212–12220.

54 S. Zeng, Y. Wang, C. Chen, H. Kim, X. Liu, M. Jiang, Y. Yu, Y. S. Kafuti, Q. Chen, J. Wang, X. Peng, H. Li and J. Yoon, *Angew. Chem.*, 2024, **136**, e202316487.

55 M. Dirak, C. M. Yenici and S. Kolemen, *Coord. Chem. Rev.*, 2024, **506**, 215710.